A new technique for curved rod bending tests based on Digital Image Correlation and its application to human ribs

S. García-Vilana[a] *, D. Sánchez-Molina[a], J. Llumà[a], J. Velázquez-Ameijide[a], C. Arregui-Dalmases[b]

July 15, 2021

[a]UPC, EEBE, Eduard Maristany, 14, 08019 Barcelona
[b]Centro Zaragoza, Crtra. 232, km.273, 50690 Pedrola

Abstract

Background. The study of the deformation of curved rods subjected to bending and its associated stress state is a complex task that has not been treated in depth in the literature, which makes difficult to obtain constitutive models or Finite Element Models (FEM) in which it is necessary to know all the components of the stress and strain tensors.

Objectives. This study focuses on a new calculation methodology to obtain stress and strain tensors of curved rods under bending.

Methods. The stress and strain tensors have been determined based on the theory of continuum mechanics and differential geometry of curves (moving bases), in a general methodology and valid for large strains, curved geometries and variable cross-sections along the specimen. This has been applied to the human rib and, in addition, a new experimental method for bending of curved specimens based on Digital Image Correlation (DIC) is presented.

Results. Both the test method and the proposed calculations applied to the human rib show results according to expectations, allowing to know the rib curvature changes along the test, the stresses and

*Corresponding author: silvia.garcia.vilana@upc.edu

strains along the rib and the components of both stress and strain in all directions, in order to build the stress and strain tensors. In addition, the results of stress, strain and young's modulus correspond to those of previous literature in tensile testing of human rib cortical bone.

Conclusions. The proposed calculations allow the construction of the strain and stress tensors of a curved specimen subjected to bending, which is of great importance for the development of constitutive models. Moreover, since with this method it is possible to calculate both tensors along the entire length of the specimen and in all directions, it is possible to apply this method in finite element models. Finally, the new test methodology allows to know the stress and strain in curved specimens such as the human rib, from bending tests.

KEYWORDS: Human rib, mechanical properties, bending testm digital image correlation.

Nomenclature

CSSR - Cross Sectional Stress Resultants (axial force, bending moments, ...)
DIC - Digital Image Correlation
FEM - Finite Element Method
mCT - micro-Computed Tomography

1 Introduction

The mechanical characterization of a biological tissue provides relevant information regarding its mechanical behavior and the load that can be applied before reaching the fracture or a permanent deformation [1, 2]. The mechanical properties are the data source for the finite element models (FEM) widely used for predicting the behavior of a solid [3, 4]. In fact, FEM include three-dimensional constitutive models developed on the basis of experimentally determined mechanical properties [5, 6], and that is the reason why simple one-dimensional constitutive relations are less useful when the general behavior of a solid needs to be known, specially in non-isotropic materials as remarked in some research studies [7].

The most common mechanical tests from which stress and strain tensors can be obtained are the tensile tests [8, 9]. However, in this type of loading the stress and strain tensors take a particularly simple form, which does not

always allow distinguishing adequately the effect of different parameters in constitutive models for nonlinear elastic materials [10, 11, 12]. Due to this fact, other tests such as bending tests can be used [13, 14, 15]. In this more complex loading situation, additional components appear in the stress and strain tensors, and this allows determining more constitutive parameters.
However, the implementation of the stress and strain tensor calculations in a bending load is not easy for materials with nonlinear constitutive equations, and the task is even more difficult if the specimen is not a straight rod and does not have constant cross-section.
A case of this type of difficulties is found for example in human bones, which present and added difficulty if they are curved, as it happens in human ribs (once the micro-cracking process is advanced). In fact, human rib has been taken as an instance of the general methodology proposed in this article. For viscoelastic or nonlinear elastic materials, the approach based in Euler or Timoshenko beam theories is not suitable, because of the intrinsic nonlinear material behavior, which is not taken into account in the ordinary beam theory. In the case of human ribs, these drawbacks are reflected, in the fact that only a limited number of constitutive parameters can be obtained, usually reduced to parameters related to properties in the direction tangent to centerline (barycentric line). In addition, many studies do not proportionate stress and strain in their tensor form [16, 17], and this limits the possibility to use these methodologies for fitting nonlinear constitutive models.
Therefore, in many cases the determination of mechanical properties is complex in curved rods under bending, but in practice, it is usually a large-strain problem that can be treated by moving frames and differential geometry of curves. This would allow the determination of stress and strain accurately and throughout the specimen.

For all the above reasons, this study focuses on the development of a new methodology for the calculation of the strain and stress tensors in curved rods under bending load and where large strain occurs. This methodology is based on the continuum mechanics theory and the differential geometry of curves for dealing with co-moving vector frames. Furthermore, this method has been applied to a widely studied, but incompletely solved case: the human rib. For this purpose, a new methodology for bending tests of curved rods, applicable to complete ribs, has been developed. In this paper, it is detailed how to compute stress and strain tensors from the displacements obtained by DIC procedures and the measured forces on the rib from a bending test for complete ribs. This kind of data make the developed methodology suitable

for finding constitutive parameters in the case of nonlinear materials, as it is experimentally shown.

2 Strain and stress calculus for planar curved rods

The three-point bending problem has been extensively analyzed by means of *beam theory*. In this kind of analysis, a dimensional reduction from 3D to 1D is carried out. This allows us to reconsider the mathematical form of the problem in terms of forces, bending moments and displacements, instead of in terms of stress and strain components. This dimensional reduction has allowed to obtain many exact analytical solutions which are very well documented in the literature for the elastic beam problem [18, 19, 20, 21, 22]. Unfortunately, classical models in beam theory (Timoshenko's and Euler's versions) assume a linear relation between stress and strain components, and for this reason are not suitable for characterizations of nonlinear materials. In addition, when DIC techniques are used, the approach based in beam theory does not provide information about the distortion of the cross-section. Even interesting works dealing with some degree of nonlinearity do not consider nonlinear constitutive equations [19, 20, 23] and due to this, this paper considers some aspects arising in the nonlinear case.

2.1 Coordinate system used for curved rods

When analyzing a curved rod, it has to be taken into account that its progressive deformation produces changes of its curvature and, thus, the geometry of the centerline varies with strain. For this reason, in a curved rod it is more appropriate to use the differential geometry of curves, i.e., the Frenet-Serret frame and its associated formulas, to deal with the change of curvature and the geometry of the barycentric line. The Frenet-Serret vector basis $\{\boldsymbol{t}, \boldsymbol{n}, \boldsymbol{b}\}$ will change in orientation between different material points on the rod and between different configurations, related to different strain levels.

For any point on the rod, $\boldsymbol{t}$ is the *tangent vector* to the barycentric line (and therefore is perpendicular to the cross-section of the rod), and the *normal* $\boldsymbol{n}$ and *binormal* $\boldsymbol{b}$ vectors are contained in the cross-section of the rod: $\boldsymbol{n}$ is directed in the vertical towards the curvature center, and $\boldsymbol{b}$ is orthogonal

to both $\boldsymbol{t}$ and $\boldsymbol{n}$, hence "bi-normal" (see Figure 1). The position of a material point on the curved rod can be defined with curvilinear coordinates (ξ, η, ζ) as the distance ξ (arc length) along the barycentric line from the coordinate origin O to the centroid of the section containing the point plus the distances η, ζ directed in the $\boldsymbol{n}$ and $\boldsymbol{b}$ directions, respectively.

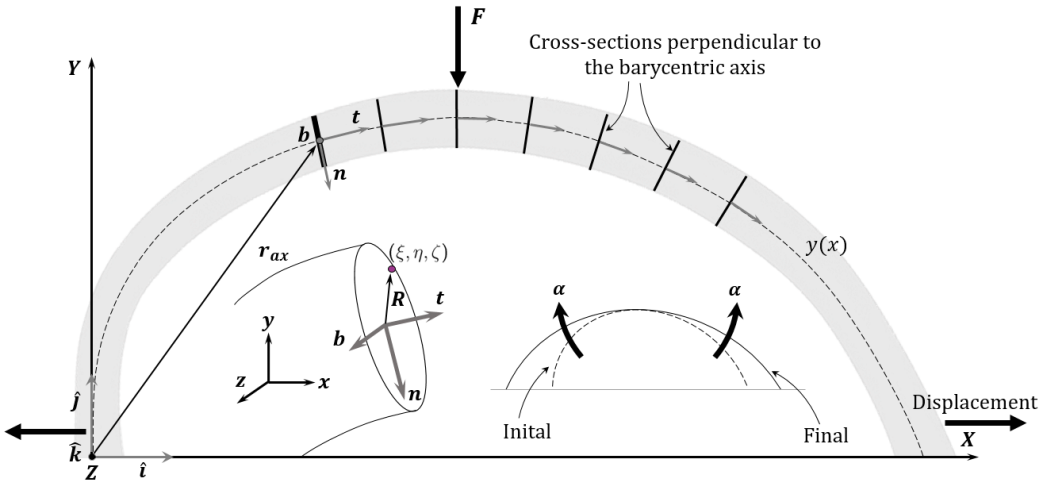

Figure 1: Location of the Frenet-Serret frame in a curved rod, applied to the rib; the frame $\{X, Y, Z\}$ is centered in the extreme of the rib and the tangent vector $\boldsymbol{t}$ is directed along the barycentric line at any point. A material point on the rib is defined with the curve coordinates (ξ, η, ζ), where ξ is the arc length from O to the centroid of the section that contains the point and η, ζ are the distances over the section in the directions $\boldsymbol{n}$ and $\boldsymbol{b}$ respectively (being $\boldsymbol{n}$ the vertical direction and $\boldsymbol{b}$ the depth direction).

It should be noticed that in a *planar problem*, the barycentric line is always contained in a plane (in this case, the XY plane). This plane is chosen to be orthogonal to the binormal vector $\boldsymbol{b}$, which is constant for a planar bending problem. In these circumstances, the barycentric line can be defined by a polynomial $y(x)$ that allows to describe its geometry and compute the vector trihedron $\{\boldsymbol{t}, \boldsymbol{n}, \boldsymbol{b}\}$, with respect to a fixed ortogonal basis $\{\hat{\boldsymbol{\imath}}, \hat{\boldsymbol{\jmath}}, \hat{\boldsymbol{k}}\}$, as:

$$\begin{aligned} \boldsymbol{t} = & \frac{1}{\sqrt{1+[y'(x)]^2}}\,\hat{\boldsymbol{i}} + \frac{y'(x)}{\sqrt{1+[y'(x)]^2}}\,\hat{\boldsymbol{j}} \\ \boldsymbol{n} = & \frac{y'(x)}{\sqrt{1+[y'(x)]^2}}\,\hat{\boldsymbol{i}} - \frac{1}{\sqrt{1+[y'(x)]^2}}\,\hat{\boldsymbol{j}} \end{aligned} \tag{1}$$

being $\boldsymbol{b} = -\hat{\boldsymbol{k}}$. The derivatives of the trihedron define the kinematic properties of a material point or particle through the Frenet-Serret formulas [24]:

$$\boldsymbol{t}' = \tau\boldsymbol{n}, \qquad \boldsymbol{n}' = -\chi\boldsymbol{t} + \tau\boldsymbol{b}, \qquad \boldsymbol{b}' = -\tau\boldsymbol{n} \tag{2}$$

where χ is the curvature and τ the torsion. When dealing with a planar situation, the torsion is $\tau = 0$ and the curvature can be computed as:

$$\chi = \frac{y''(x)}{[1+(y'(x))^2]^{3/2}} \tag{3}$$

2.2 Strain computation for curved rods

Once defined the reference system and the coordinates to be used, two configurations are considered: the *initial undeformed curve configuration* before the deformation and the *deformed configuration* after the change in shape, whose curvature has varied. Let us assume then that the deformation from one curve to the next deformed curve involves an intermediate configuration in which the rod has been unbent (*reference configuration*), see Figure 2.

The transitions from the reference configuration to the initial and the deformed configurations can be defined with the mappings φ_0 and φ respectively:

$$\begin{cases} (\xi,\eta,\zeta) \mapsto \varphi_0(\xi,\eta,\zeta) & = \boldsymbol{R}(\xi,\eta,\zeta) & = \boldsymbol{R}_{ax}(\xi) + \eta\boldsymbol{N}(\xi) + \zeta\boldsymbol{B}(\xi) \\ (\xi,\eta,\zeta) \mapsto \varphi(\xi,\eta,\zeta) & = \boldsymbol{r}(\xi,\eta,\zeta) & = \boldsymbol{r}_{ax}(\xi) + \Lambda(\eta)[\eta\boldsymbol{n}(\xi) + \zeta\boldsymbol{b}(\xi)] \end{cases} \tag{4}$$

being $\{\boldsymbol{T},\boldsymbol{N},\boldsymbol{B}\}$ and $\{\boldsymbol{t},\boldsymbol{n},\boldsymbol{b}\}$ the basis vectors of the Frenet-Serret frame in the initial and deformed configurations respectively, $\boldsymbol{R}$ and $\boldsymbol{r}$ the point position and $\boldsymbol{R}_{ax}$, $\boldsymbol{r}_{ax}$ the position of the centroid of the cross-section containing the material point. The kinematic hypothesis for deformation under bending used in equation (4) is similar to the results used in asymptotic analysis of elastic curved rods [19, 21]. The function $\Lambda(\eta)$ describes the distortion of the

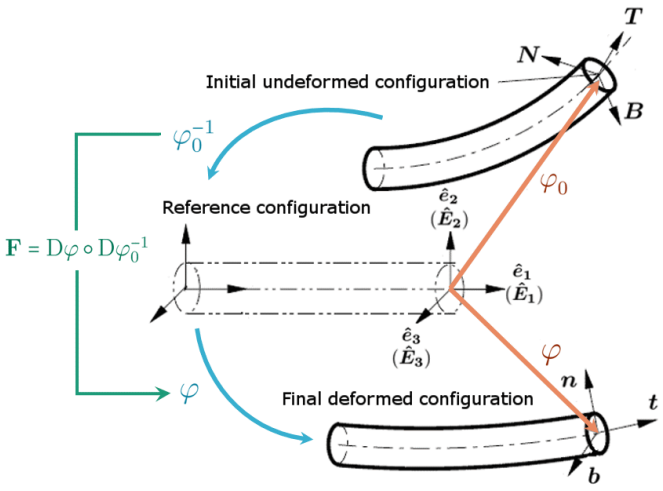

Figure 2: Schematic view of the three configurations used: (top) initial undeformed configuration, (center) [straight] reference configuration and (bottom) deformed configuration. The mappings ϕ_0 and ϕ apply the reference configuration in the undeformed configuration and the deformed configuration respectively.

cross-section due to the Poisson effect, and it will be computed later. For the moment, it is advanced that the function $\Lambda(\eta)$ is representable by a power series of the form:

$$\Lambda(\eta) = 1 + \sum_{k=1}^{\infty} f_k(\bar{\nu})(\chi - \chi_0)^k \eta^k \tag{5}$$

with $\bar{\nu} = \bar{\nu}(\lambda)$ a Poisson function which depends on the maximum stretch λ in the cross-section. Inside the summation term, χ is the curvature in a deformed configuration, χ_0 the initial curvature (in the undeformed configuration) and $f_k(\bar{\nu})$ are functions to be determined that satisfy $f_k(0) = 0$ [for a linear isotropic elastic material $\bar{\nu}$ reduces to ordinary Poisson ratio ν_0]. We will see in equation (15) that this conjectured form for $\Lambda(\eta)$ is correct.

From the kinematic hypothesis (4), the deformation gradient $\mathbf{F} = (F^i_J) = (\partial r^i / \partial \theta^J)$ can be computed as the composition $\mathbf{F} = \mathrm{D}\varphi \circ \mathrm{D}\varphi_0^{-1}$ of both mappings, where $\mathrm{D}(\bullet)$ denotes the Jacobian matrix of a mapping. The columns of the Jacobian matrix are defined as $\boldsymbol{U_i}$ for the initial mapping φ_0 and $\boldsymbol{u_i}$ for the final (spatial) mapping φ and correspond to the derivatives of $\boldsymbol{R}$ and $\boldsymbol{r}$ with respect to the coordinates $(\theta^1, \theta^2, \theta^3) = (\xi, \eta, \zeta)$ respectively.

The Jacobian matrix of the map φ is given by:

$$\mathrm{D}\varphi = \left[\frac{\partial r^i}{\partial \theta^j}\right] = [\boldsymbol{u_1}, \boldsymbol{u_2}, \boldsymbol{u_3}] = \left[\boldsymbol{t} + \Lambda\eta\boldsymbol{n'} + \Lambda\zeta\boldsymbol{b'},\ \left(\Lambda + \frac{\partial\Lambda}{\partial\eta}\eta\right)\boldsymbol{n} + \frac{\partial\Lambda}{\partial\eta}\zeta\boldsymbol{b},\ \Lambda\boldsymbol{b}\right] \tag{6}$$

where $\boldsymbol{u_i}$ represent column vectors forming together the Jacobian matrix $\mathrm{D}\varphi$. Introducing the well known Frenet-Serret formulas (2) and the planarity condition $\tau = 0$:

$$\mathrm{D}\varphi = [\boldsymbol{u_1}, \boldsymbol{u_2}, \boldsymbol{u_3}] = \left[(1 - \Lambda\eta\chi)\boldsymbol{t},\ \left(\Lambda + \frac{\partial\Lambda}{\partial\eta}\eta\right)\boldsymbol{n} + \frac{\partial\Lambda}{\partial\eta}\zeta\boldsymbol{b},\ \Lambda\boldsymbol{b}\right] \tag{7}$$

Following the same steps for the φ_0 mapping, with torsion $\tau_0 = 0$, and operating its inverse:

$$\begin{aligned} \mathrm{D}\varphi_0^{-1} = \left[\frac{\partial R^J}{\partial \theta^j}\right]^{-1} &= \frac{1}{1 - \eta\chi_0}[\boldsymbol{U_2} \times \boldsymbol{U_3}, \boldsymbol{U_3} \times \boldsymbol{U_1}, \boldsymbol{U_1} \times \boldsymbol{U_2}]^{\mathrm{T}} \\ &= \frac{1}{1 - \eta\chi_0}[\boldsymbol{T},\ (1 - \eta\chi_0)\boldsymbol{N},\ (1 - \eta\chi_0)\boldsymbol{B}]^{\mathrm{T}} \end{aligned} \tag{8}$$

The composition of both matrices allows us to obtain:

$$\mathbf{F} = \frac{1 - \Lambda\eta\chi}{1 - \eta\chi_0}\,\boldsymbol{t} \otimes \boldsymbol{T} + \left(\Lambda\boldsymbol{n} + \eta\frac{\partial\Lambda}{\partial\eta}\,\boldsymbol{n}\right) \otimes \boldsymbol{N} + \zeta\frac{\partial\Lambda}{\partial\eta}\,\boldsymbol{b} \otimes \boldsymbol{N} + \Lambda\,\boldsymbol{b} \otimes \boldsymbol{B} \tag{9}$$

Now to compute the above expression in the spatial basis $\{\boldsymbol{t}, \boldsymbol{n}, \boldsymbol{b}\}$, we observe that vector basis the Frenet–Serret trhiedron in initial configuration is nothing more than a rotation of the deformed basis given by an angle α (see Figure 1), and $\boldsymbol{B} = \boldsymbol{b}$, therefore:

$$\begin{aligned} \mathbf{F} = \ & \frac{1 - \Lambda\eta\chi}{1 - \eta\chi_0}\,\boldsymbol{t} \otimes (\cos\alpha\ \boldsymbol{t} - \sin\alpha\ \boldsymbol{n}) + \left(\Lambda\boldsymbol{n} + \frac{\partial\Lambda}{\partial\eta}\eta\boldsymbol{b}\right) \otimes (\sin\alpha\ \boldsymbol{t} + \cos\alpha\ \boldsymbol{n}) + \ldots \\ & \cdots + \zeta\frac{\partial\Lambda}{\partial\eta}\,\boldsymbol{b} \otimes (\sin\alpha\ \boldsymbol{t} + \cos\alpha\ \boldsymbol{n}) + \Lambda\ \boldsymbol{b} \otimes \boldsymbol{b} \end{aligned} \tag{10}$$

In order to simplify the above expression, we define a curvature change factor κ, as:

$$\kappa := \frac{1-\Lambda\eta\chi}{1-\eta\chi_0} \tag{11}$$

Using the parameter κ, the spatial components of the deformation gradient given in equation (10) can be written as:

$$\mathbf{F}_s = \begin{bmatrix} \kappa\cos\alpha & -\kappa\sin\alpha & 0 \\ (\Lambda+\eta\Lambda')\sin\alpha & (\Lambda+\eta\Lambda')\cos\alpha & \zeta\Lambda' \\ (\eta+\zeta)\Lambda'\sin\alpha & (\eta+\zeta)\Lambda'\cos\alpha & \Lambda \end{bmatrix} \tag{12}$$

From this form, the (spatial) Eulerian–Almansi strain tensor $\boldsymbol{\varepsilon}^{(s)} = (\mathbf{I} - \mathbf{F}_s^{-\mathrm{T}}\mathbf{F}_s^{-1})/2$ is given by:

$$\boldsymbol{\varepsilon}^{(s)} = \frac{1}{2}\begin{bmatrix} 1-\dfrac{1}{\kappa^2} & 0 & 0 \\ 0 & 1-\dfrac{\Lambda^2}{p_2^2(\Lambda,\Lambda')}-\dfrac{(\eta+\zeta)^2\Lambda'}{p_2(\Lambda,\Lambda')} & \dfrac{\Lambda'\Lambda\zeta}{p_2^2(\Lambda,\Lambda')}+\dfrac{p_1(\Lambda,\Lambda')(\eta+\zeta)\Lambda'}{p_2(\Lambda,\Lambda')} \\ 0 & \dfrac{\Lambda'\Lambda\zeta}{p_2^2(\Lambda,\Lambda')}+\dfrac{p_1(\Lambda,\Lambda')(\eta+\zeta)\Lambda'}{p_2(\Lambda,\Lambda')} & -\dfrac{(\zeta\Lambda')^2}{p_2^2(\Lambda,\Lambda')}+\dfrac{p_1^2(\Lambda,\Lambda')}{p_2(\Lambda,\Lambda')} \end{bmatrix} \tag{13}$$

where the polynomials $p_1(\Lambda,\Lambda')$ and $p_2(\Lambda,\Lambda')$ have the form:

$$\begin{cases} p_1(\Lambda,\Lambda') = & \Lambda+\Lambda'\eta \approx \Lambda, \\ p_2(\Lambda,\Lambda') = & \Lambda(\Lambda+\Lambda'\eta)-\zeta(\eta+\zeta)\Lambda'^2 \approx \Lambda^2 \end{cases}$$

When $|(\chi-\chi_0)\eta| << 1$ the above approximations in the last equations hold, if $\Lambda(\eta) >> \eta\Lambda'(\eta)$ and $\Lambda(\eta) >> \zeta\Lambda'(\eta)$. In the same approximation regime, the Eulerian–Almansi strain tensor reduces to:

$$\boldsymbol{\varepsilon}^{(s)} \approx \frac{1}{2}\begin{bmatrix} 1-\dfrac{1}{\kappa^2} & 0 & 0 \\ 0 & 1-\dfrac{1}{\Lambda^2} & 0 \\ 0 & 0 & 1-\dfrac{1}{\Lambda^2} \end{bmatrix} \tag{14}$$

The above equation is asymptotically valid for a curved rod of nonlinear isotropic material (or of transversally isotropic material where the preferred direction is tangent to the centerline, which is the case for human ribs).

Because of the Poisson effect in a bending situation we have $\varepsilon_{yy}^{(s)} = \varepsilon_{yy}^{(s)} = -\bar{\nu}\varepsilon_{xx}^{(s)}$ and this conditions allow to find the function $\Lambda(\eta)$:

$$1 - \frac{1}{\Lambda^2} = -\bar{\nu}\left(1 - \frac{1}{\kappa^2}\right)$$

Because of the equation (11) for κ, the above equation leads to a fourth-degree polynomial equation in Λ. But since we depart from the asymptotically valid equation (14), keeping the same order of approximation, the following aproximation for $\kappa \approx (1 - \eta\chi)/(1 - \eta\chi_0)$ is used, obtaining the convenient asymptotic equation:

$$\Lambda(\eta) \approx \frac{\tilde{\kappa}}{\sqrt{1 + (1 + \bar{\nu})(\tilde{\kappa}^2 - 1)}} = \frac{1 - \chi\eta}{1 - \chi_0\eta}\left[1 + (1 + \bar{\nu})\left(\frac{(1 - \chi\eta)^2}{(1 - \chi_0\eta)^2} - 1\right)\right]^{-1/2} \tag{15}$$

For a linear elastic material, $\bar{\nu}$ reduces to the Poisson ratio; but for a nonlinear material it takes a specific form associated with a plane stress state for the planar rod (see section 7). Now, it is clear by calculating the Taylor series in η that the function $\Lambda(\eta)$ has the mathematical form (5), as it was claimed.

2.3 Stress computation for curved rods

In the calculation of stress from forces, we encounter a difficulty: Navier's formula for the calculation of stresses from CSSR (axial force and bending moments) is not valid for a nonlinear material. This makes it impossible to determine the stress components σ_{ij} directly from the section resultants, i.e., axial force and bending moments. This difficulty can be overcome by calculating the CSSR directly from the strains and the parameters of the *constitutive equation* of the elastic material (every Cauchy elastic material admits a constitutive equation), so one has, for example, that:

$$\sigma_{xx} = f(\varepsilon_{ij}^s; \mu_1, \ldots, \mu_n) = \bar{f}_{\mu_k}(\varepsilon_{ij}^s) \tag{16}$$

where ε_{ij}^s is the spatial Eulerian–Almansi strain tensor and μ_k are the constitutive parameters that are intended to be determined through the bending test. For an isotropic or transversely isotropic nonlinear elastic material with deformation given by (14), the above relationship leads to an equation of the form:

$$\sigma_{xx} = \bar{f}_{\mu_k}(\varepsilon^s_{xx}, \varepsilon^s_{yy}, \varepsilon^s_{zz}) = \bar{f}_{\mu_k}(\varepsilon^s_{xx}, -\bar{\nu}\varepsilon^s_{xx}, -\bar{\nu}\varepsilon^s_{xx}) =: F_{\mu_k}(\varepsilon^s_{xx}) \tag{17}$$

The equations (14) and (11) allow us to express the stress as a function of the current curvature, the initial curvature, and the coordinate η along the radii of curvature:

$$\sigma_{xx} = F_{\mu_k}\left(\frac{1}{2}\cdot\frac{1-\Lambda\eta\chi}{1-\eta\chi_0}\right) \tag{18}$$

The function F_{μ_k}, typically, is a known function with unknown constitutive parameters $(\mu_1, \ldots, \mu_n)$ and the bending test is intended to determine the values of such parameters. This objective can be achieved considering that the axial force and bending moments as a function of the constitutive parameters:

$$\begin{aligned}
\hat{N}_x^{(\mu_k)} &= \int_\Omega F_{\mu_k}\left(\frac{1-\Lambda\eta\chi}{2(1-\eta\chi_0)}\right)\,\mathrm{d}\eta\mathrm{d}\zeta \\
\hat{M}_\eta^{(\mu_k)} &= \int_\Omega F_{\mu_k}\left(\frac{1-\Lambda\eta\chi}{2(1-\eta\chi_0)}\right)\zeta\,\mathrm{d}\eta\mathrm{d}\zeta \\
\hat{M}_\zeta^{(\mu_k)} &= -\int_\Omega F_{\mu_k}\left(\frac{1-\Lambda\eta\chi}{2(1-\eta\chi_0)}\right)\eta\,\mathrm{d}\eta\mathrm{d}\zeta
\end{aligned} \tag{19}$$

Then, the parameters $(\mu_1, \ldots, \mu_n)$ can be found by minimizing the function:

$$\Phi(\mu_1, \ldots, \mu_n) = \sum_{j=1}^{N}\left[(N_x^{(j)} - \hat{N}_x^{(\mu_k)})^2 L_a^2 w^2 + (M_\zeta^{(j)} - \hat{M}_\zeta^{(\mu_k)})^2 + (0 - \hat{M}_\eta^{(\mu_k)})^2\right] \tag{20}$$

Thus, the difficulty of determining the stress from CSSR in a straightforward way can be circumvented by directly minimizing those forces and moments, rather than trying to approximate the stress with a Navier-like formula. Notice that in the above *residue function* Φ, we have taken into account that, for a rod bent in the plane, it is expected that $M_\eta^{(j)} = 0$. In the above formula, the length L_a has been introduced to homogenize dimensionally the function Φ (the factor w is an adimensional "weight" calibrated to ensure a good fitting, and L_a can be chosen as $L_a^2 =$ area).

Once the constitutive parameters $(\mu_1, \ldots, \mu_n)$ have been determined, the stress σ_{xx} can be calculated a posteriori from the constitutive equation (16).

In addition, in many cases the complexity of the equations (19) can be avoided by considering a Taylor series for $\Phi(\mu_k)$ (see appendix section 8). Moreover, for a thin wall structure like a rib, the effect of nonlinearity in the stress is limited because the third area moments are very low, see example computations in the appendix.

2.4 Application to human ribs

The characterization of the human rib has been well studied in recent years [9, 25, 26, 27], but the mechanical properties of bending tests in the literature are based on the linear elastic theory of beams and ignore the distortion of the cross-section. These two factors combined can produce large departure in the computation of the actual stress and strain in a sample.
In addition, the human rib has a remarkable and non-constant curvature, as well as a variation of the cross-section along the centerline [28]. That is why most of the research, both in human rib bending tests and in other curved samples, is focused on the determination of the mechanical properties in the fracture section once its location is known, without the chance to calculate these values in other points of the material before the failure. Moreover, given the difficulty of testing curved samples as in the case of the rib, many experimental designs are based on tests of rib sections or the placement of supports whose position on the rib varies throughout the test.
Many of the above difficulties can be solved using computations for initial curved rods in the regime of semi-large strain regime, see section 7.

3 Data and methods

3.1 Materials

Human rib specimens were harvested from forensic autopsies conducted at the *Forensic Pathology Service* of the *Legal Medicine and Forensic Science Institute of Catalonia* (IMLCFC), which were initially removed for complementary medico-legal investigation. This study was approved by the Research and Ethics committee of IMLCFC. For this study, the entire 4th rib of post-mortem human subjects was used. Some human ribs were used for showing how the previous methodology works for curved bones. For the empirical validation of the methodology, a total of 17 ribs from 10 PMHS were

used: 7 male and 3 female individuals (from some individuals, both left and right ribs were used). The average age of the subjects was 51±11 years (from 26 to 62 years) and body mass index (BMI) of 30.4± 5.4 kg/m^2. Prior to the experimental tests, the soft tissue and cartilage was removed.

3.2 Experimental tests

For the bending test considered in this study, the entire ribs were subjected to three-point bending tests following a new test methodology. The aim of this test is to allow a free sliding and opening of the rib extremes in order to determine the maximum displacements and deflections along the rib and compute the stress and strain. An overview of the experimental test is shown in Figure 3.

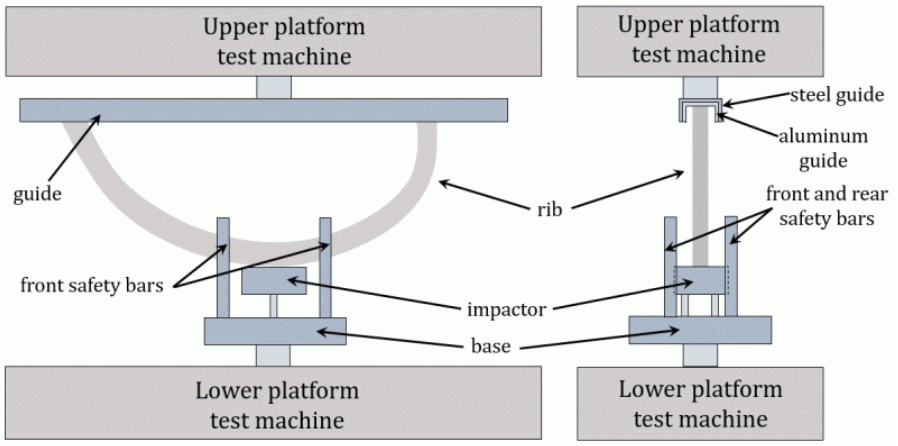

Figure 3: Bending test scheme: the rib is placed in the plane, with its extremes inside the guide and the outer middle region in contact with the impactor. Safety bars protect against the rib slipping out of the plane.

The bending tests were performed with a Zwick® ProLine 20 and loads were measured with a load cell of 2000 N coupled to a data acquisition system (Spider 8-30 from HBM®). The experimental setting consisted of a guide placed in the upper platform of the test machine, where the extremes of the rib are introduced, and an impactor placed in the lower platform, which applies the force in the outer middle region of the rib, so that the extremes of the rib slide along the guide. The upper U guide was made of steel, inside

which an aluminum guide was fixed to reduce the friction of the rib ends when sliding. To minimize friction, the guide was kept lubricated, and the rib ends were coated with polytetrafluoroethylene band. On the other hand, the lower assembly consisted of an aluminum prismatic base to which a prismatic impactor was attached. This type of impactor was chosen because in previous tests with cylindrical impactors, localized damage was detected that induced a stress concentration, locally damaging the sample; however, the objective of this experimental test was to calculate the maximum stress of the rib in the macroscopic fracture. In addition, four aluminum bars were fixed to the prismatic base to provide protection to the test in case of a lateral slide of the rib (the bars were never in contact with the sample).
The whole test was recorded with a high-speed camera and the video was then processed following a DIC procedure with MATLAB® to determine the displacements of the selected points along the contour of the rib during the test and to compute the strain tensor as explained in the following sections.

The objective of this experimental testing was to show that the basic mechanical properties obtained from the proposed bending test methodology do not differ significantly from a similar sample of coupons machined from the cortical part of the ribs and tested in tensile tests. The 83 specimens used for tensile tests were the same specimens considered in some previous papers of the same authors [12].
The comparison of the results obtained from the two different testing methodologies is intended to show the adequacy of the new proposed bending methodology. In addition, in some cases, the more complex stress-strain state produced in bending allows to distinguish some constitutive parameter that in a tensile test can be confused.

3.3 Digital Image Correlation procedure

The bending test is recorded in video, and for each video frame a set of specific points or landmarks are tracked by means of DIC procedures using a MATLAB® script. Remarkably the script was originally developed for a different experimental setting related to tensile test[10, 12]; however a clever use of the DIC procedures allows use it for the bending test as explained in sections 2.1 and 2.2 thanks to the formulas of differential geometry of curves.

Specifically, for application of the DIC procedure, the video was decompressed in frames, and in the first frame of the test a line mesh of points was

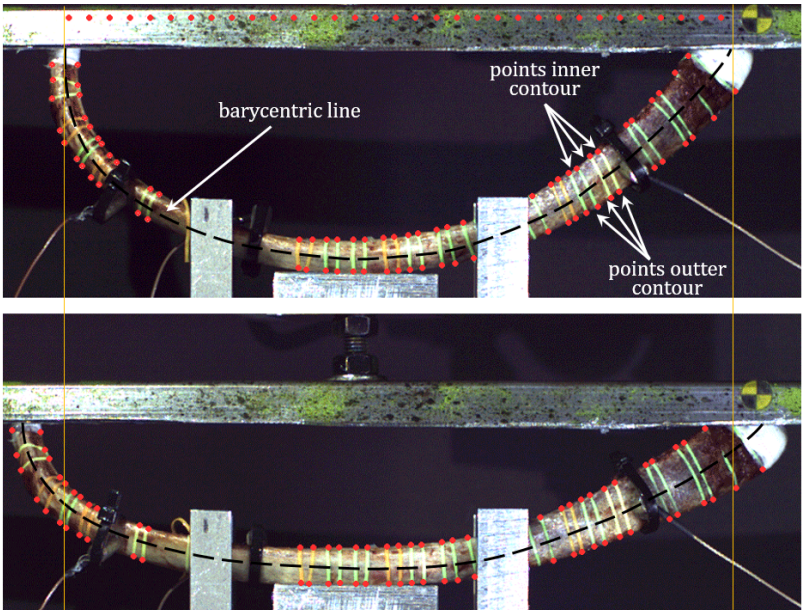

Figure 4: Points defined for the motion tracking with DIC procedures; line of points defined on the guide and at the intersections of the inner and outer contours of the rib with the rubber bands.

created on the guide to determine its position at each moment. On the other hand, to compute the displacements of the rib, different points or landmarks were defined over in the inner and outer contours of the rib to be tracked by the software. For this purpose, before the test some elastic bands were placed in different positions of the rib, to allow the tracking of their positions along the test (see Figure 4). With the use of a Computerized Tomography (CT) of human rib it has been verified that the error committed in considering the barycentric line as the middle point of the contours is 3%, whose maximum error corresponds to 0.4 mm at the central region where the rib breaks. Thus, the intersections of each elastic band with the upper and lower contours of the rib were tracked by the software, and the middle position of each pair of elastic band intersections was considered to belong to the barycentric line. Those set of the mentioned positions was known in each frame, thus defining the geometry of the barycentric line of the rib throughout the test.

3.4 Specific computations for strain and stress

An accurate computation of the strain requires computing adequately the barycentric line. The barycentric line of the rib in each testing time t was approximated by a polynomial $y_t(x)$ fitted to the points whose positions define the barycentric line. On the basis of the positions of each point of the centerline, the tangent $\boldsymbol{t}$ and normal $\boldsymbol{n}$ vectors, as well as curvature ξ were determined.

The CSSR could be computed from the reactions in the extremes of the rib of each deformed configuration. Defining L_x as the horizontal distance between the ends of the rib, we have $L_x = a + b$ and being a the longitudinal distance from the anterior end to the application location of the vertical force F and b the distance from the force application to the posterior end. The reactions were $\boldsymbol{R_p} = Fb/L_x\ \hat{\boldsymbol{j}}$ and $\boldsymbol{R_a} = Fa/L_x\ \hat{\boldsymbol{j}}$ and so:

$$\begin{aligned} 0 \le x < a: &\quad N_x = \boldsymbol{R_p}\cdot\boldsymbol{t}, \quad V_\eta = \boldsymbol{R_p}\cdot\boldsymbol{n}, \quad M_\zeta = \boldsymbol{R_p}\ x \\ a \le x < b: &\quad N_x = \boldsymbol{R_a}\cdot\boldsymbol{t}, \quad V_\eta = \boldsymbol{R_a}\cdot\boldsymbol{n}, \quad M_\zeta = \boldsymbol{R_a}x + \boldsymbol{F}(x-a) \end{aligned} \tag{21}$$

Being N_x the axial force, V_η the shear force and M_ζ the bending moment. With these data, a fitting procedure can be carried out by minimizing a function of the same form as Φ defined in (20). The strain tensor in the fracture region was calculated using equations (14).

On the other hand, for computing explicitly the stress a previous fitting of the constitutive parameters from the CSSR is required. Then, from these parameters, the stress can be computed from constitutive equation (16).

4 Results

The proposed bending methodology has been implemented to 4th level human rib bending tests from deceased human subjects to obtain data comparable with other testing methodologies, and to assess the adequacy of the proposed procedures. The 4th human rib can be a represented as a curved rod [mainly] contained in a plane. The selected coordinate system is shown in the Figure 1 and all the computations are implemented in that coordinate frame. In the bending tests, the ends of the ribs were coated with polytetrafluoroethylene bands and kept lubricated to reduce friction and introduced

in a U guide contained in the plane containing the centerline of the 4th rib. The test force of bending was directly applied on the central outer surface of the rib and, as the force increases, the rib ends freely slide in opposite directions along the guide, resulting in a change in shape. The positions of the midpoints of the rubber bands along the test were obtained by following the DIC procedure described in the previous section (see Figure 4). As shown in Figure 4, the geometry of the rib changes as the load increases. This change of geometry is represented in Figure 5(a), where it can be seen the initial barycentric line of the rib (y_0), the barycentric line after a certain test time when the load increased (y_f real), and this same central line which was rescaled in length X to the initial length in order to compare the changes in curvature between both initial and deformed configurations (y_f). In Figure 5(b), the curvature of the barycentric line along the rib for the initial (χ_0) and deformed (χ) configurations is represented. As it can be seen, the higher decreases in curvature are observed in three regions along the rib, which are indicated in Figure 5, where the maximum curvature decrease occurs in the central region of the rib. Around this three regions, the rib is being straightened as the bending force increases.

The spatial strain tensor $\boldsymbol{\varepsilon}^{(s)}$ and the Cauchy stress tensor $\boldsymbol{\sigma}$ were calculated. For the strain tensor, only the components $\varepsilon_{xx}^{(s)}, \varepsilon_{yy}^{(s)}$ and $\varepsilon_{zz}^{(s)}$ are non-zero, while $\varepsilon_{xy}^{(s)} = \varepsilon_{xz}^{(s)} = \varepsilon_{yz}^{(s)} = 0$. Using the proposed procedure, all those components can be computed for any point of the rib once the geometrical parameters are known. The higher strain and stress occur in the upper and lower fibers of the rib, being the longitudinal $\varepsilon_{xx}^{(s)}$ component those of maximum values with respect to the other components.

To show the results obtained from the proposed calculation procedure, the inner fiber of the rib was used. The strain tensor in each point defined by the rubber bands was computed using its particular geometrical properties, which vary in each section. Curvature was previously computed in each time of the test and each point along the barycentric line and η was the distance from the barycentric line to the upper fiber.
Figure 6(a) shows the deformation profile along the upper fiber of the rib, whose position is indicated by the horizontal initial position X. As expected, the profile is similar to that of curvature change (Figure **??**). In Figure 6(b), the strain values are plotted versus the change in curvature, and there is a

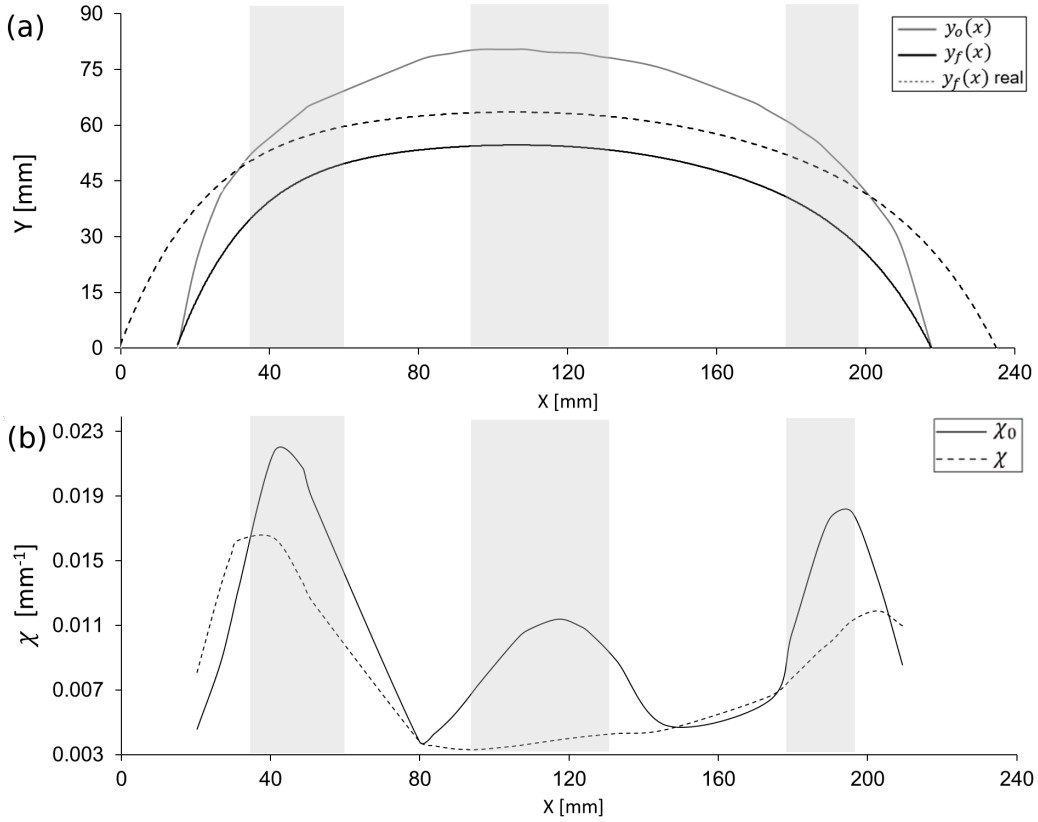

Figure 5: (a) Initial (gray line), deformed (black dot line) and deformed rescaled (black line) configurations of the rib. The three regions of maximum curvature variation are represented with the gray zones, whose maximum variation corresponds to the dotted vertical lines. (b) Curvature of the rib along the barycentric line, represented with the horizontal position between the extremes; initial curvatures χ_0 before increasing the load and Final curvatures χ once the maximum force is achieved.

clear correlation between curvature change and strain as expected. On the other hand, axial and shear forces, as well as bending moment, were computed for each time of the test and along the whole rib. With these data and the geometrical parameters, the stress component $\sigma_{xx}^{(s)}$ was obtained, being the rest of the components negligible. The axial stress profile for the final load is shown in Figure 7. As it can be seen, the maximum principal stress is reached near the point where the force is applied. The shear component, ignored in equation (14), was computed using the well-known Collignon–Jorawski formula to ensure its value is not relevant compared to the axial

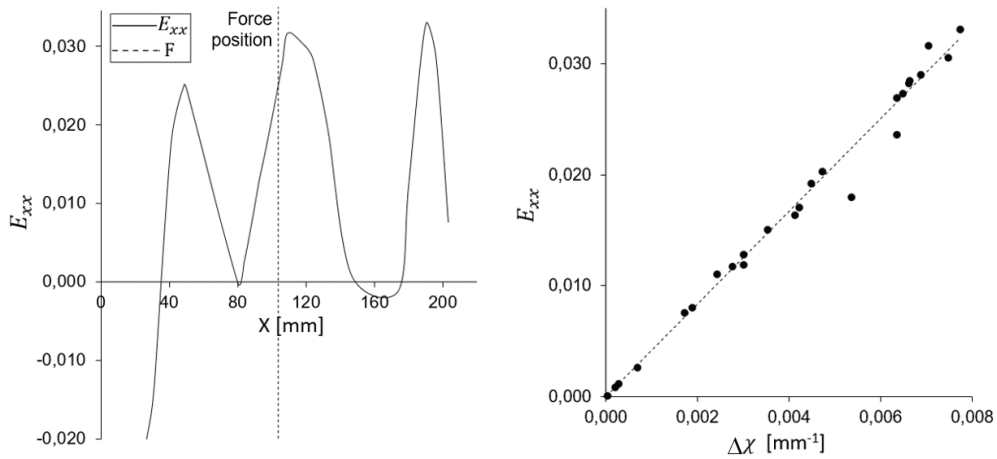

(a) (b)

Figure 6: (a) Final longitudinal strain in each position along the rib and load application position. (b) Plot of final longitudinal strain along the rib and increase in curvature from the initial configuration and trend line. The maximum strain occur at the points where the curvature changes the most.

stress. The shear stress did not exceed in any case 6± 0.6% times the axial stress, and can be neglected for determining the principal stress σ_I. In the present case $\sigma_I = (\sigma_{xx} + \sqrt{\sigma_{xx}^2 + 4\sigma_{xy}^2})/2 < 1,005\sigma_{xx}$.

From the values of strain and stress during the whole test, the stress-strain curves and main mechanical properties can be obtained. The Young modulus of different bending tests of ribs were computed from the slope of the elastic region of the stress-strain curves of the fracture section. The results obtained for bending tests were compared with tensile test results from *coupons* (dog-shape) manufactured from cortical rib bone in complementary studies [12], which were contrasted with the literature. The average values of the mechanical properties of tensile and bending tests are represented in Figure 8. It can be seen that the mechanical properties of bending tests are similar to those obtained for tensile tests. The strain value obtained is 176±62 MPa, within the range of the values of 153–185 MPa obtained by other studies [17, 26]. The same is observed with the Young modulus, which average value is 15.4±5.6 GPa, being the literature values of those studies of 11.9–20 GPa.

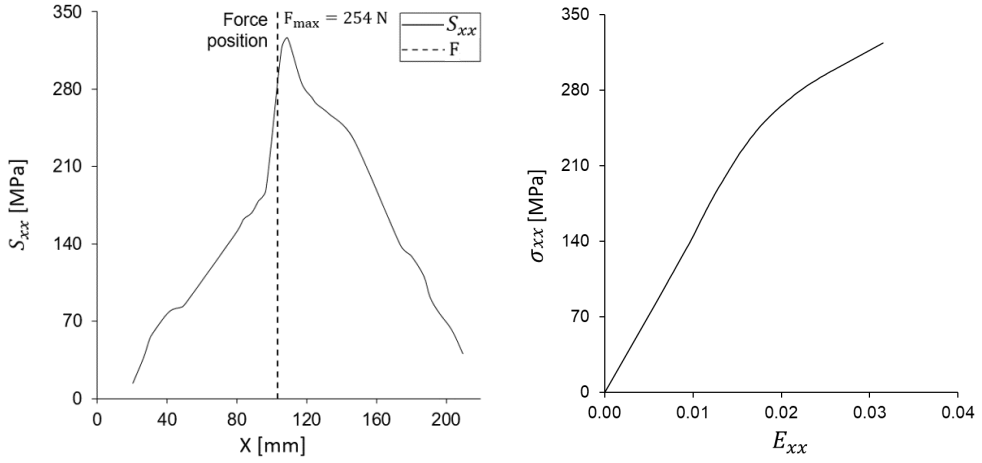

Figure 7: (a) Axial stress profile along the upper contour of the rib. (b) Stress-strain curve using the principal components of both tensors in the central section of the rib, corresponding to the fracture section.

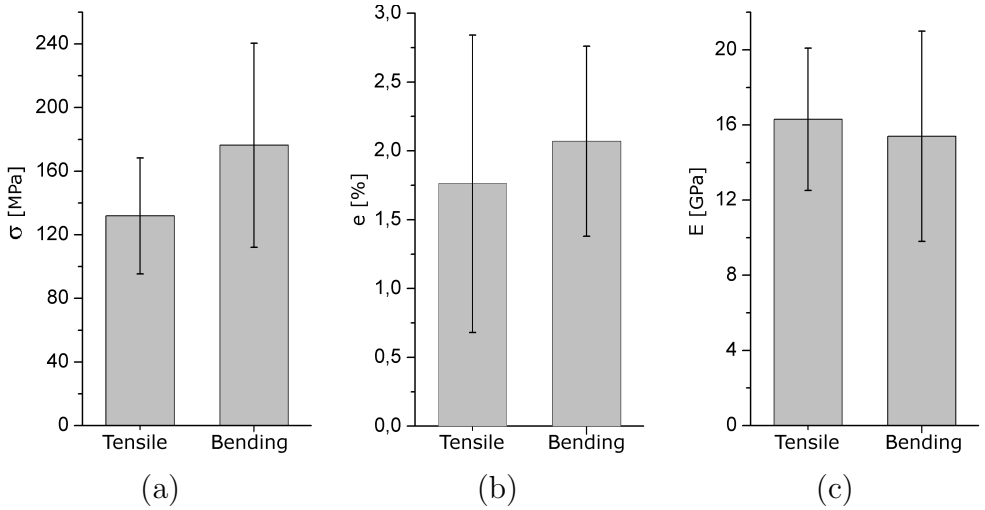

Figure 8: (a) Axial stress, (b) axial strain and (c) Young Modulus average values for both tensile and bending rib tests. As it can be seen, the results obtained by the two methods seem comparable.

Moreover, stress-strain curves for tensile and bending tests are reported in Figure 9. As it can be seen, bending curves are similar to tensile plots.

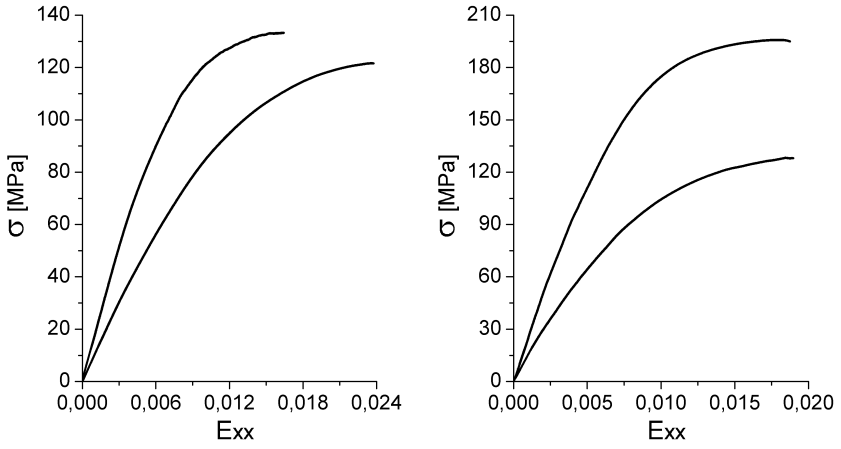

Figure 9: Stress-strain curves for the axial components of (a) tensile and (b) bending tests.

5 Discussion

Bending tests are a simple alternative to tensile tests for estimating the Young's modulus of a material. They can also be used when the maximum strains are small and the nonlinearity of the material is small, since in all these cases the Infinitesimal Strain Theory can be used. However, when the stress distribution over a cross-section is far away from linearity, then Navier's formula itself is no longer valid and many other formulas based on it do not work properly. So the ultimate stress σ_u and other magnitudes can be inaccurate.

However, some studies based on bending tests seem to assume that Navier's formula is valid in general [13, 29, 30, 32], even when the material is nonlinear elastic. Nevertheless, this assumption may not be adequate for materials with nonlinear behavior and only provides a reasonably approximate result for a small strain regime. Some recent works have insisted on the importance of directly relating the curvature to the bending moment by looking for nonlinear relationships [31], leaving aside Navier's formula, in the same line as the work developed here that seeks to relate the curvature directly to the bending moments. In our work the peculiarity is that we use Finite Strain Theory and the use of Navier's formula is avoided. An excellent discussion of how Navier's formula should be modified to obtain more accurate and re-

alistic stress distributions is given in [33]. These types of ideas are not only of theoretical interest, there are some papers that use nonlinear bending for various applications [34].

On the other hand, in this work it has been seen that the curves obtained for simple tensile tests, based on [35], provide values for the mechanical properties that do not differ significantly from those obtained by the new bending methodology, see Figure 9.
The crucial difference is that obtaining specimens for tensile tests requires a lot of machining time to fabricate coupons of the right size and shape, whereas the bending tests, although they have slightly more complex post-processing, it can be automated and this experimental setting do not require machining on the rib.
In addition, the stress-strain state induced in a bending test is less symmetric that the state induce in a tensile test, this in principle allows to distinguish the effects of different constitutive parameters, which in a tensile situation may appear as lumped in with others. In addition, the bending test developed induces a non-uniform stress-strain state, so one has cross-sections with different levels of stress appear on the same rod, whereas in a tensile test the stress-strain state is always homogeneous, which makes it difficult to force the macroscopic failure to being in a specific region of the rod for example. This could be interesting for developing failure models for materials.

6 Conclusion

This paper proposes a bending test methodology, which with certain restrictions, even allows dealing with problems outside the small-strain regime. Moreover, the proposed methodology can be implemented even in materials with a nonlinear stress-strain response.
To illustrate how the methodology works, an experimental design has been made with human ribs, which during the loading process undergo microcracking before macroscopic failure. The results of this test show that the new methodology produces mechanical property values equivalent to those obtained by tensile testing. In addition, the most of the samples in this study were used in combination with Acoustic Emission Data to develop a fracture model of ribs, where the methodology in this paper was used for the mechanical testing [36].

References

[1] Carretta, R., Stüssi, E., Müller, R. & Lorenzetti, S. (2013). "Within subject heterogeneity in tissue-level post-yield mechanical and material properties in human trabecular bone", *Journal of the mechanical behavior of biomedical materials*, **24**, pp. 64–73.

[2] Nyman, J. S., Granke, M., Singleton, R. C. & Pharr, G. M. (2016). "Tissue-level mechanical properties of bone contributing to fracture risk", *Current osteoporosis reports*, **14**(4), pp. 138–150.

[3] Mullins, L. P., Bruzzi, M. S. & McHugh, P. E. (2009). "Calibration of a constitutive model for the post-yield behaviour of cortical bone", *Journal of the Mechanical Behavior of Biomedical Materials*, **2**(5), pp. 460–470.

[4] Ng, T. P., Koloor, S. S. R., Djuansjah, J. R. P. & Kadir, M. A. (2017). "Assessment of compressive failure process of cortical bone materials using damage-based model", *Journal of the Mechanical Behavior of Biomedical Materials*, **66**, pp. 1–11.

[5] Miller, K. (1999). "Constitutive model of brain tissue suitable for finite element analysis of surgical procedures", *Journal of biomechanics*, **32**(5), pp. 531–537.

[6] Hashash, Y. M. A., Jung, S. & Ghaboussi, J. (2004). "Numerical implementation of a neural network based material model in finite element analysis", *International Journal for numerical methods in engineering*, **59**(7), pp. 989–1005. (2004). . , 59(7), 989-1005.

[7] Bischoff, J. E., Arruda, E. M. & Grosh, K. (2000). "Finite element modeling of human skin using an isotropic, nonlinear elastic constitutive model", *Journal of biomechanics*, **33**(6), pp. 645–652.

[8] Garcia, D., Zysset, P. K., Charlebois, M. & Curnier, A. (2009). "A three-dimensional elastic plastic damage constitutive law for bone tissue.", *Biomechanics and modeling in mechanobiology*, **8**(2), pp. 149–165.

[9] Li, S., Demirci, E. & Silberschmidt, V. V. (2013). "Variability and anisotropy of mechanical behavior of cortical bone in tension and compression", *Journal of the mechanical behavior of biomedical materials*, **21**, pp. 109–120.

[10] Sánchez-Molina, D., Velázquez-Ameijide, J., Quintana, V., Arregui-Dalmases, C., Crandall, J.R., Subit, D., Kerrigan, J.R. (2013). "Fractal dimension and mechanical properties of human cortical bone", *Medical engineering & physics*, **35**(5), pp. 576–582.

[11] Atsumi, N., Tanaka, E., Iwamoto, M. & Hirabayashi, S. (2017). "Constitutive modeling of cortical bone considering anisotropic inelasticity and damage evolution", *Mechanical Engineering Journal*, **4**(4), pp. 17–00095.

[12] Velázquez-Ameijide, J., García-Vilana, S., Sánchez-Molina, D., Llumà, J., Martínez-González, E., Rebollo-Soria, M. C. & Arregui-Dalmases, C. (2020). "Prediction of mechanical properties of human rib cortical bone using fractal dimension", *Computer Methods in Biomechanics and Biomedical Engineering*, pp. 1–11.

[13] Albert, C. I., Jameson, J., & Harris, G. (2013). "Design and validation of bending test method for characterization of miniature pediatric cortical bone specimens." *Proceedings of the Institution of Mechanical Engineers, Part H: Journal of Engineering in Medicine*, **227**(2), pp. 105–113.

[14] Bradley, A. L., Swain, M. V., Waddell, J. N., Das, R., Athens, J. & Kieser, J. A. (2014). "A comparison between rib fracture patterns in peri-and post-mortem compressive injury in a piglet model", *Journal of the mechanical behavior of biomedical materials*, **33**, pp. 67–75.

[15] Agnew, A. M., Schafman, M., Moorhouse, K., White, S. E. & Kang, Y. S. (2015). "The effect of age on the structural properties of human ribs. Journal of the mechanical behavior of biomedical materials", *Journal of the mechanical behavior of biomedical materials*, **41**, pp. 302–314.

[16] Stitzel, J. D., Cormier, J. M., Barretta, J. T., Kennedy, E. A., Smith, E. P., Rath, A. L. & Duma, S. M. (2003). "Defining regional variation in the material properties of human rib cortical bone and its effect on fracture prediction", *Stapp Car Crash Journal*, **47**, pp. 243–265.

[17] Kemper, A. R., McNally, C., Pullins, C. A., Freeman, L. J. & Duma, S. M. (2007). "The biomechanics of human ribs: material and structural properties from dynamic tension and bending tests", *Stapp Car Crash Journal*, **51**, pp. 235–273.

[18] Stump, D. M. & Van Der Heijden, G. H. M. (2000). "Matched asymptotic expansions for bent and twisted rods: applications for cable and pipeline laying." *Journal of engineering mathematics*, **38**(1), pp. 13–31.

[19] Scardia, L. (2006). "The nonlinear bending–torsion theory for curved rods as Γ-limit of three-dimensional elasticity", *Asymptotic Analysis*, **47**(3-4) pp. 317–343.

[20] Scarpello, G. M., & Ritelli, D. (2011). "Exact solutions of nonlinear equation of rod deflections involving the Lauricella hypergeometric functions", *International Journal of Mathematics and Mathematical Sciences*, 2011.

[21] Vetyukov, Y. (2014). "Plane Bending of a Curved Rod", *Nonlinear Mechanics of Thin-Walled Structures*, pp. 37–70.

[22] Fogang, V. (2020). "Timoshenko Beam Theory Exact Solution For Bending, Second-Order Analysis, and Stability" (pre-print).

[23] Brunetti, M., Favata, A., & Vidoli, S. (2020). "Enhanced models for the nonlinear bending of planar rods: localization phenomena and multistability". *Proceedings of the Royal Society A*, **476**(2242), 20200455.

[24] Mate, A. (2017). "The Frenet-Serret Formulas." *Brooklyn Collage Of The City University Of New York, izdano*, 19.

[25] Currey, J. D. (2004). "Tensile yield in compact bone is determined by strain, post-yield behaviour by mineral content", *Journal of biomechanics*, **37**(4), pp. 549–556.

[26] Cormier, J. M., Stitzel, J. D., Duma, S. M. & Matsuoka, F. (2005). "Regional variation in the structural response and geometrical properties of human ribs", *In Annual Proceedings/Association for the Advancement of Automotive Medicine*, **49**, pp. 153.

[27] Kerrigan, J. R., Sanchez-Molina, D., Neggers, J., Arregui-Dalmases, C., Velazquez-Ameijide, J. & Crandall, J. R. (2014). "Indentation response of human patella with elastic modulus correlation to localized fractal dimension and bone mineral density", *Journal of the mechanical behavior of biomedical materials*, **33**, pp. 99–108.

[28] Mohr, M., Abrams, E., Engel, C., Long, W. B. & Bottlang, M. (2007). "Geometry of human ribs pertinent to orthopedic chest-wall reconstruction", *Journal of biomechanics*, **40**(3), pp. 1310–1317.

[29] Fukuda, H. (1989). "A new bending test method of advanced composites." *Experimental Mechanics*, **29**(3), pp. 330–335.

[30] Bencardino, F. (2013). "Mechanical parameters and post-cracking behaviour of HPFRC according to three-point and four-point bending test." *Advances in Civil Engineering*, 2013.

[31] Liang, B., Chaudet, P., & Boisse, P. (2017). "Curvature determination in the bending test of continuous fibre reinforcements." *Strain*, **53**(1), e12213.

[32] Marks, M. R., Cheong, K. Y., & Hassan, Z. (2018). "An improved three-point bending test method for the investigation of nanosecond laser dicing of ultrathin Si dies with Cu stabilization layer." *Materials Characterization*, **136**, pp. 29–40.

[33] Polizzotto, C. (2015). "From the Euler–Bernoulli beam to the Timoshenko one through a sequence of Reddy-type shear deformable beam models of increasing order." *European Journal of Mechanics-A/Solids*, **53**, pp. 62-74.

[34] Liu, T., Li, Z. M., & Jin, S. (2018). "Nonlinear bending analysis of anisotropic laminated tubular beams based on higher-order theory subjected to different kinds of distributed loads." *International Journal of Pressure Vessels and Piping*, **163**, pp. 23–35.

[35] Velázquez-Ameijide, J., García-Vilana, S., Sánchez-Molina, D., Martínez-González, E., Llumà, J., Rebollo-Soria, M.C., & Arregui-Dalmases, C. (2021). "Influence of anthopometric variables on the mechanical properties of human rib cortical bone." *Biomedical Physics & Engineering Express*, **7**(3), 035013.

[36] García-Vilana, S., Sánchez-Molina, D., Llumà, J., Fernández-Osete, I., Velázquez-Ameijide, J., & Martínez-González, E. (2021). "A predictive model for fracture in human ribs based on Acoustic Emission Data", *Medical Physics*, **48**(9), pp. 5540–5548.

[37] Saravia, C. M. (2014). "A large deformation–small strain formulation for the mechanics of geometrically exact thin-walled composite beams", *Thin-Walled Structures*, **84**, pp. 443–451.

[38] Bhatti, A. Q., Kishi, N., Mikami, H., & Ando, T. (2009). "Elasto-plastic impact response analysis of shear-failure-type RC beams with shear rebars", *Materials & Design*, **30**(3), pp. 502–510.

7 Supplement: On the semi-large strain regime

In the scientific literature concerning continuous media, it is common to differentiate among large-strain problems and small-strain problems.

Mathematically, this difference is that large-strain problems refer to problems which are studied using a strain tensor which is obtained by means of a nonlinear differential operator of the displacements, and small strain problems refer to approaches which use the strain tensor obtained with linear operators of the displacements [37].

On the other hand, large-strain regime and small-strain regime are informally used to refer to the magnitude of the strain. It is obvious that situations with large strain require the use of nonlinear operators of the displacements in order to preserve accuracy, and small-strain situations can be adequately approximated with linear operators. No clear difference between these two regimes has been established. In this paper, a conventional difference is proposed: the stress-strain around a point will be called in the small-strain regime when the full nonlinear Green-Lagrange strain tensor (expressed in the material coordinates) does not differ more than a 5% from the infinitesimal strain tensor, a slightly lower limit than the margins of error considered in ordinary structural engineering [38].

This study considered some approximations by ignoring shear stress and making some asymptotic approximations using strain tensor (14) instead of full strain tensor (13). However, even with these approximations the proposed procedure allows dealing with large-strain regime in the conventional sense described in the previous paragraph, using an approximated nonlinear

strain tensor with simplifications. The approximations in section 2.2 are typically under the margin of 5% as longer the magnitude $|(\chi-\chi_0)\eta| < 0.05$ even being the actual principal strain larger than 5% greater than the computed infinitesimal strain. We propose to denominate this kind of situation, when some asymptotic approximations are used, but the strain components are large a *semi-large strain approach*.

8 Appendix: Approximations for section forces and moments

In section 2.3, the exact formulas for computing the axial force and bending moments from the strain field along the cross-section of a rod are deduced, see equation (19). When the constitutive model is highly nonlinear the computation can be extremely cumbersome. In some cases, a Taylor approximation is useful for obtaining successive approximations to the constitutive parameters. For example, if we consider a second order Taylor series for $F_{\mu_k}(\varepsilon_{xx}) \approx a\varepsilon_{xx} + b\varepsilon_{xx}^2$, an approximation could be obtained involving not only second area moments but also third order area moments. In this case:

$$\begin{aligned}\sigma_{xx} &\approx \left(\frac{1-\Lambda\eta\chi}{2(1-\eta\chi_0)}\right) + b\left(\frac{1-\Lambda\eta\chi}{2(1-\eta\chi_0)}\right)^2 \\ &\approx a(\chi_0-\chi)\eta + [(3a-2b)\chi + (2b-a)\chi_0](\chi_0-\chi)\frac{\eta^2}{2}\end{aligned}$$

Then using this approximation in equation (19):

$$\begin{aligned} N_x &\approx [(3a-2b)\chi + (2b-a)\chi_0](\chi_0-\chi)I_{\boldsymbol{b}} \\ 0 &\approx a(\chi_0-\chi)I_{\boldsymbol{bn}} + [(3a-2b)\chi + (2b-a)\chi_0](\chi_0-\chi)J_1 \\ M_\zeta &\approx -a(\chi_0-\chi)I_{\boldsymbol{b}} - [(3a-2b)\chi + (2b-a)\chi_0](\chi_0-\chi)J_2 \end{aligned} \tag{22}$$

where two third area moments have appeared:

$$J_1 = \int_\Omega \eta^2\zeta \ \mathrm{d}\eta\mathrm{d}\zeta, \qquad J_2 = \int_\Omega \eta^3\zeta \ \mathrm{d}\eta\mathrm{d}\zeta$$

For the computations of the area moments some mCT of human ribs can be used. These mCT were processed using the sub-package BoneJ® implemented in the software ImageJ®, obtaining the geometrical data along the

rib, such as cross-sections, area moments, thicknesses among other values useful in the above computations.
Finally, by minimizing the function $\rho(a, b)$ for all the times t_j:

$$\rho(a,b) = \sum_j \left[L_a^2 (N_x^{exp}(t_j) - N_x(t_j))^2 + (M_\zeta^{exp}(t_j) - M_\zeta(t_j))^2 + (0 - M_\eta(t_j))^2 \right]$$

with respect to a and b one obtains an approximate solution for these parameters, for obtaining a more accurate solution a higher order series needs to be used.